DROPWISE CONDENSATION ON HYDROPHILIC SURFACES

BY

ALEX WU

THESIS

Submitted in partial fulfillment of the requirements
for the degree of Master of Science in Mechanical Engineering
in the Graduate College of the
University of Illinois at Urbana-Champaign, 2018

Urbana, Illinois

Adviser:

Professor Nenad Miljkovic

ABSTRACT

Droplet nucleation and condensation are ubiquitous phenomena in nature and industry. Over the past century, research has shown dropwise condensation heat transfer on non-wetting surfaces to be an order of magnitude higher than filmwise condensation heat transfer on wetting substrates. However, the necessity for non-wetting to achieve dropwise condensation is unclear. Here we report stable dropwise condensation on a smooth, solid, hydrophilic surface (θ_a = 38°) having low contact angle hysteresis (< 3°). We show that the distribution of droplet sizes for coalescing droplets agrees well with the classical distribution on hydrophobic surfaces. Our findings demonstrate that achieving stable dropwise condensation is not governed by surface intrinsic wettability, as assumed for the past eight decades, but rather it is dictated by contact angle hysteresis [0].

TABLE OF CONTENTS

INTRODUCTION

Droplet nucleation and condensation are ubiquitous phenomena in nature and industry. Over the past century, research has shown that heat transfer rates during dropwise condensation on non-wetting (e.g., hydrophobic) surfaces can be 20X higher than filmwise condensation on wetting substrates [1,2]. However, the need for non-wetting hydrophobic coatings in achieving dropwise condensation of water is unclear. Sustained dropwise condensation requires continuous droplet removal from the surface. High mobility of droplets on the surface facilitates easy droplet removal. The mobility of a droplet on a surface is governed by the contact angle hysteresis (i.e., the difference between the advancing and receding contact angles) [3-8] rather than the intrinsic wettability of the surface. While all prior work on achieving dropwise condensation has focused on employing hydrophobic surfaces, we postulate that achieving dropwise condensation on a hydrophilic surface with low contact angle hysteresis is theoretically possible. Dropwise condensation on hydrophilic surfaces has additional advantages including enhanced nucleation rate (Fig. 1a) due to reduced energy barriers for droplet nucleation (Fig. 1a, inset) [9], lower conduction thermal resistance for surfaces with advancing contact angles $\theta_a \ll 90°$ [10], and higher (~ 500%) heat transfer coefficient (Fig 1b) compared to hydrophobic surfaces. Furthermore, droplet shedding and mobility due to gravitational forces becomes invariant to intrinsic surface wettability as the contact angle hysteresis approaches zero (Fig. 1c, inset), ensuring enhanced heat transfer is maintained even for hydrophilic substrates (Fig. 1c). Here, we report the first-ever stable dropwise condensation on a solid hydrophilic surface (θ_a = 38°) having minimal contact angle hysteresis (< 3°). Using optical microscopy and macroscale photography, we studied the nucleation site distribution on the hydrophilic substrate, showing

that the distribution of droplet sizes for coalescing droplets agrees remarkably well with the classical distribution on hydrophobic surfaces. Based on our findings, we show that dropwise condensation, rather than being governed by the surface intrinsic wettability or advancing contact angle, as assumed for the past eight decades, is dictated by the contact angle hysteresis, the minimization of which induces stable dropwise condensation. This work not only provides fundamental insights into dropwise condensation theory, but shows a previously unexplored avenue to achieving anti-fouling, anti-corrosion, self-cleaning, anti-bacterial, and enhanced heat transfer surfaces through the use of non-classical approaches to easily remove liquid in the condensed or deposited phase.

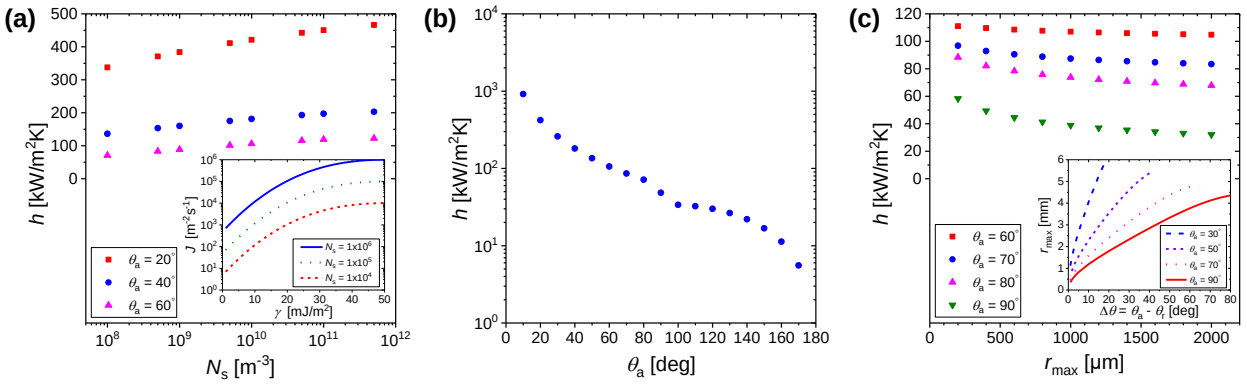

Figure 1. Parameters affecting condensation heat transfer coefficient (h). Model results showing influence of: (a) nucleation density for varying advancing contact angle θ_a and r_{max} = 1 mm, Inset: Condensation nucleation rate (J) as a function of condensing surface energy (γ), (b) advancing contact angle with nucleation density N_s = 5 x 10^{10} m^{-2} and departure radius r_{max} = 1 mm, and (c) departure radius for varying advancing contact angle θ_a and nucleation densityN_s= 5 x 10^{10} m^{-2}, Inset: Theoretical sliding droplet radius (r_{max}) as a function of contact angle hysteresis ($\Delta\theta$). The results assume a vapor pressure of 3500 Pa and surface temperature of 20°C. Results show that hydrophilic dropwise condensation is advantageous to hydrophobic.

Maintaining a high intrinsic wettability (i.e., $\theta_a \ll 90°$) with minimal contact angle hysteresis is difficult to achieve. Many studies have noted the formation of discrete 'flat' water droplets on hydrophilic substrates during condensation due to atmospheric contamination of volatile organic compounds after cleaning [11], however the corresponding receding contact angle is typically close to zero [12], resulting in film formation and filmwise condensation once droplet coalescence ensues [13]. Hence, for the past eight decades, dropwise condensation of water has been achieved mainly via the deposition of hydrophobic conformal coatings, typically having a non-polar alkyl or perfluoroalkyl chemistry with high advancing and receding contact angle ($\theta_a \approx 125°$, $\theta_r > 90°$) and low contact angle hysteresis. However, as the contact angle hysteresis approaches zero, the minimum droplet sliding size becomes invariant to intrinsic surface wettability (Fig. 1c, inset). Consequently, we postulate that the performance of hydrophilic surfaces with low contact angle hysteresis in dropwise condensation is at least comparable to that of hydrophobic surfaces. However, these predictions are yet to be reconciled experimentally.

EXPERIMENTAL DETAILS

For the PEGylated surfaces, silicon wafers (<1 0 0> orientation) were cut to 2 cm × 2 cm, cleaned by sonication in acetone and ethanol, rinsed with deionized (DI) water and dried with nitrogen. For PEGylation, cleaned silicon wafers were exposed to oxygen plasma (PlasmaEtch) for 15 min and subsequently immersed in a solution consisting of 1 μl of 2-[Methoxy(polyethyleneoxy)6-9propyl]trimethoxysilane and 8 μl of hydrochloric acid in 10 ml of anhydrous toluene for 18 hours at room temperature. Finally, the PEGylated surfaces were rinsed thoroughly with anhydrous toluene, ethanol and DI water and stored in DI water for further use.

To synthesize our hydrophobic surfaces, smooth silicon wafers (P-type, <1 0 0> orientation, 0-100 Ohm-cm, single side polished) were used as the base substrate. The wafers were first cleaned with acetone, isopropyl alcohol (IPA), DI water, and then dried with nitrogen. The wafers were de-scummed by oxygen plasma (Jupiter March RIE, 150 W) for 2 minutes to remove all remaining organic residues. After cleaning the surfaces completely, a conformal layer of octafluorocyclobutane (C_4F_8) was coated on the surfaces by chemical vapor deposition using STS-DRIE to uniformly functionalize the surfaces to be hydrophobic. The thickness of C_4F_8 was proportional to deposition time, and 3 minute deposition yielded about 100 nm thickness.

Our hydrophilic surfaces began with smooth silicon wafers (P-type, <1 0 0> orientation, 0-100 Ohm-cm, single side polished) that were cleaned with acetone, IPA, DI water, and then dried with nitrogen. Afterwards, the wafers were treated with air plasma for 10 minutes before being left out uncovered in a lab environment in Urbana, IL (40°06′14″N, 88°12′44″W) to adsorb hydrocarbons and volatile organic compounds for 1 week [14-17].

We began creating our hydrophobic copper surfaces with smooth, single side polished copper tabs that were cleaned with acetone, IPA, DI water, and then dried with nitrogen. Afterwards, the copper tabs were treated with air plasma for 10 minutes before being left out uncovered in a lab environment in Urbana, IL (40°06′14″N, 88°12′44″W) to adsorb hydrocarbons and volatile organic compounds for 1 week [14-17].

XPS analysis was conducted on the surfaces using a PHI-5800 spectrometer (Physical Electronics). XPS was conducted using a monochromatic Al Kα X-ray source operated at 15 kV and photoelectrons were collected at a takeoff angle of ≈45° relative to the sample surface. At least 30 different locations were analyzed to assess the chemical homogeneity of the PEGylated surfaces. The surface morphology and the surface roughness of the substrates were characterized with AFM (Bruker MultiMode 8-HR). AFM was conducted with silicon nitride probes mounted on cantilevers in the ScanAsyst® mode. AFM images were acquired by scanning 5 μm x 5 μm areas on the PEGylated surfaces in air, under ambient laboratory conditions, at a scan rate of 1 Hz. The images were analyzed with NanoScope Analysis 1.8 software to obtain the root mean square roughness R_{rms}. At least 30 different locations were analyzed to assess the roughness of the PEGylated surfaces. The contact angles were measured using a contact angle goniometer (Rame-Hart 200-F1). The contact angles were measured by advancing or receding ~8 μL droplets on the surface. At least six measurements were performed on each surface. Contact angle measurements of ≈ 100 nL droplets on all samples were performed using a microgoniometer (MCA-3, Kyowa Interface Science). At least six measurements were performed on each surface.

Figure 2 shows a schematic of the condensation experimental setup [18]. The sample was attached to a Peltier based thermal plate (TP104SC, Instec), herein called the cold stage, using

heat transfer tape (McMaster). The cold stage was connected to a temperature controller (mK2000, Instec) that held the cold plate at 0.05 ± 0.1°C. A second water bath of DI-water was heated to 73 ± 3°C using a hot plate. Compressed nitrogen was supplied at the bottom of the second bath water tank at a low flow rate. While rising through the hot water the nitrogen gas saturated with water vapor and was then guided through two thermally insulated ¼" pipes to the sample surface. The outlets of the pipes were arranged vertically at a center-center distance of 0.3–0.5 in. The resulting condensation area spanned roughly 1 in horizontally and 0.7 in vertically and represented the top-most area of a vertical pate. All condensation experiments were done in ambient conditions 23°C, 50% relative humidity). The presence of noncondensable gases (NCGs) was not a concern since steady-state droplet size distribution densities have been shown to be independent of the concentration of NCGs. A Canon EOS 7D Mark II camera captured images of the condensing water droplets at a resolution of 5472 x 3648 pixels. A telephoto lens (70–300 mm, Tamron) was set to 70 mm and infinity focus. To achieve various levels of magnification with a total range of droplet radii from 10 to 1000 μm, a 5X (TU Plan Fluor EPI, Nikon), 10X (TU Plan Fluor EPI, Nikon), and 20X (TU Plan Fluor EPI, Nikon) magnification infinity focus microscope lenses with stepdown adapters were attached to the regular telephoto lens.

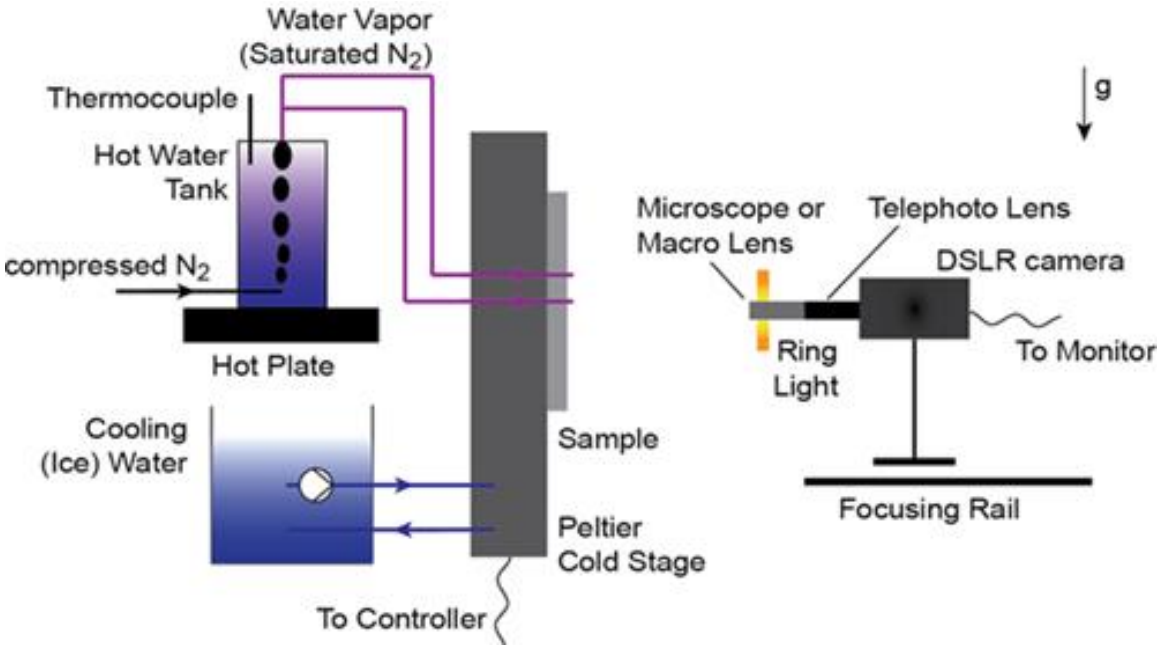

Figure 2. Schematic of the condensation experimental setup. Steam carried by saturated N_2 and supplied to the sample at two vertically stacked locations condensed on the sample attached to a Peltier cold stage. A DSLR camera was equipped with a regular 70–300 mm telephoto lens and an additional microscope or macro lens. A ring light supplied uniform lighting.

For droplet radii larger than 1000 µm, a macro lens (MP-E 65mm, Canon) set to 1X magnification was used. Videos with a 100X lens (TU Plan Fluor EPI, Nikon) on an optical microscope (Nikon LV100 upright) were used to determine the nucleation site density of droplets. Table 1 lists the pixel distance calibration for the different lens combinations with still photographs. For calibration, the outer diameter of a gauge 33 needle or 10 mm Si pillars were measured and compared to the number of pixels within the feature. The sample was illuminated with a LED ring light (LED-144-YK, AmScope). The camera and lens setup were placed on a macro rail and fine linear translation stage (PT1, Thor labs) to allow image focusing. To make focusing easier, the camera was connected to an external monitor. Due to a very shallow depth of focus for high magnification shots, it was crucial to perfectly align the camera to the sample. Any tilt (vertically or horizontally) resulted in droplets that were out of focus and the automated droplet detection software (MATLAB, Python) failed.

Table 1. Lens calibration table

Lens	Calibration (μm/pixel)
Macro	4.26
5X	2.13
10X	1.05
20X	0.52
100X	0.09

To capture droplet data during all stages of a sweeping period and to ensure statistical significance, we captured one image every 20 s. A minimum of 80 images were analyzed for each lens combination. The steady state distributions of droplet sizes were measured with these images, and the resulting distributions were used to find the droplet number density $N(R)$ as a function of droplet radius. The nucleation site droplets were counted in the direct condensation regime just before coalescence started. The reported values are an average of at least 15 swept areas. Overall, we estimate the error associated with the automated droplet detection to be less than 10%.

In order to experimentally reconcile our predictions, and to investigate what governs dropwise condensation, we fabricated smooth, slippery hydrophilic surfaces through PEGylation of silicon wafers. Our PEGylated surfaces enable the formation of water droplets with relatively low intrinsic advancing contact angles, while maintaining minimal contact angle hysteresis ($\Delta\theta = \theta_a - \theta_r$). Macroscopic water droplets deposited on our precisely engineered PEGylated surfaces displayed advancing and receding contact angles of θ_a = 38 ± 1° and θ_r = 35 ± 1°, respectively (Fig. 3a, $\Delta\theta \approx 3°$), enabling minimal contact line pinning and easy shedding [5]. Microscale goniometric measurements (MCA-3, Kyowa Interface Science Ltd.) of droplets on our PEGylated silicon wafer showed advancing and receding contact angles of θ_a = 38.6 ± 0.6° and θ_r = 36 ± 0.7°, respectively ($\Delta\theta \approx 2°$). The low contact angle hysteresis on our PEGylated

surfaces is due to the high degree of chemical homogeneity (i.e., uniform surface modification) and physical homogeneity (i.e., low surface roughness) [6-8]. High-resolution C1s XPS spectra (see Fig. 3b) at multiple (> 30) locations showed the presence of a peak at 286.5 eV corresponding to the –C–O bond, implying high degree of chemical homogeneity [19]. Further, topographical characterization with atomic force microscopy (AFM) indicated that our PEGylated surfaces had very low root mean square roughness, $R_{\mathrm{rms}} \approx 0.25$ nm (see Fig. 3c), implying high degree of physical homogeneity. Although the recent development of lubricant infused surfaces (LISs or SLIPSs) have shown the concurrent minimization of intrinsic surface contact angle and contact angle hysteresis for low surface tension condensates such as alkanes [20], this was not achieved with water as the working fluid which still showed hydrophobic states ($\theta_{\mathrm{a}} > 90°$) [10].

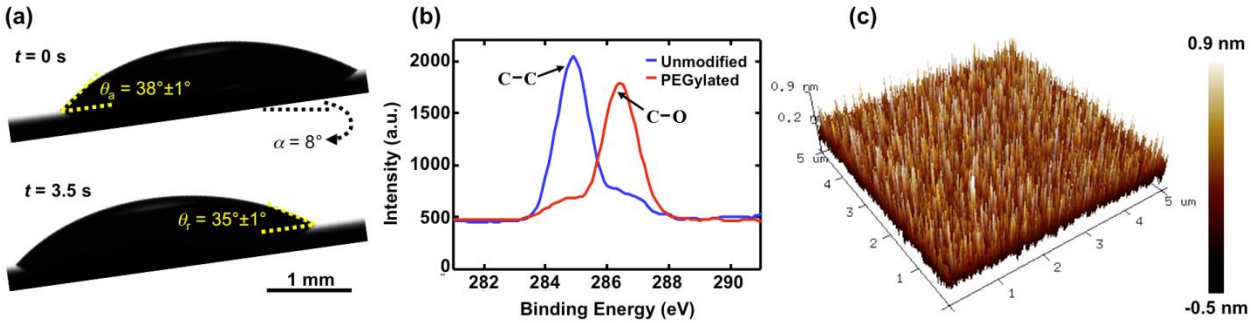

Figure 3. Surface characteristics and wettability. (a) Images showing a water droplet sliding across our PEGylated surfaces tilted by 8° relative to the horizontal. (b) High-resolution C1s XPS spectra of the unmodified and our PEGylated surfaces. The –C–C peak on an unmodified silicon wafer is due to adventitious carbon [21,22]. The –C–O peak on our PEGylated surface is indicative of PEGylation. (c) AFM image depicting the topography of our PEGylated surface with root mean square roughness, $R_{\mathrm{rms}} < 1$ nm.

The nucleation, growth, and coalescence of condensing water droplets was studied by condensing water vapor either from the ambient laboratory environment, or from a saturated

vapor supply on our PEGylated surfaces having temperatures T_w = 5 ± 0.5°C. To compare the condensation dynamics on our PEGylated hydrophilic surfaces with classical dropwise condensation dynamics on hydrophobic surfaces, we also fabricated identical smooth silicon surfaces functionalized with a fluorinated polymer (C_4F_8) deposited using chemical vapor deposition under low pressure at room temperature. This process allows for the development of a highly conformal, but thin (≈100 nm) polymer layer. Microscale goniometric measurements of droplets on the hydrophobic silicon wafer showed advancing and receding contact angles of θ_a = 110 ± 4° and θ_r = 102 ± 5°, respectively.

EXPERIMENTAL RESULTS

Droplet nucleation studies using optical microscopy revealed the formation of discrete droplets on our hydrophilic PEGylated surfaces. Details of the optical microscopy setup can be found else ware [23-25]. Due to the hydrophilic nature of the surface, the initial nucleation density, prior to droplet coalescence mediated growth, was higher on the hydrophilic surface ($n \leq$ 2.23 x 10^{10} droplets/m^2) when compared to the hydrophobic reference ($n \leq$ 2.47 x 10^9 droplets/m^2), in agreement with classical nucleation theory. Interestingly, once droplet coalescence initiated between neighboring droplets on our hydrophilic PEGylated surface, analogous transitions to larger discrete droplets ensued and dropwise condensation was maintained. In order to study the behavior of interacting hydrophilic droplets, the nucleation density on our PEGylated surface was elevated by increasing the saturation temperature of the incoming vapor supply to T_{air} = 35 ± 0.5°C and relative humidity to $\Phi \approx$ 100 ± 1%. The increased saturation temperature resulted in a supersaturation ($S = [\Phi P_{\mathrm{sat}}(T_{\mathrm{air}})]/P_{\mathrm{sat}}(T_{\mathrm{w}})$) increase from S = 1.02 ± 0.035 to S = 8.56 ± 0.4, and a corresponding increase in the nucleation rate and active nucleation site density to $N \geq$ 4 x 10^{12}, consistent with nucleation site activation [9]. At the elevated nucleation densities, the center-to-center spacing between neighboring droplets was as low as ≈500 nm. Surprisingly, the formation of discrete droplets was stable on our hydrophilic PEGylated surface, with discrete droplets having radii as small as R = 300 ± 150 nm.

To study the scale dependency of discrete droplet formation and stability of dropwise condensation, we quantified the droplet distribution density during condensation on a vertical flat plate. Briefly, the sample was attached to a Peltier based cold stage, at 0.05 ± 0.1°C. Saturated

water vapor was sparged from a second water bath of DI-water at 73 ± 3°C. The resulting condensation area spanned roughly 2.5 cm horizontally and 1 cm vertically and represented the top-most area of a vertical pate. All condensation experiments were done in ambient conditions (≈23°C, 50 ± 5% relative humidity). To capture droplet data during all stages of a sweeping period and to ensure statistical significance, we captured one image every 10–15 s. Figure 4 shows the self-similar nature for both hydrophilic PEGylated and hydrophobic surfaces with low contact angle hysteresis. Interestingly, on both hydrophobic (Fig. 4a, b) and hydrophilic (Fig. 4c, d) surfaces, all droplets remained as spherical caps and dropwise condensation ensued without film formation.

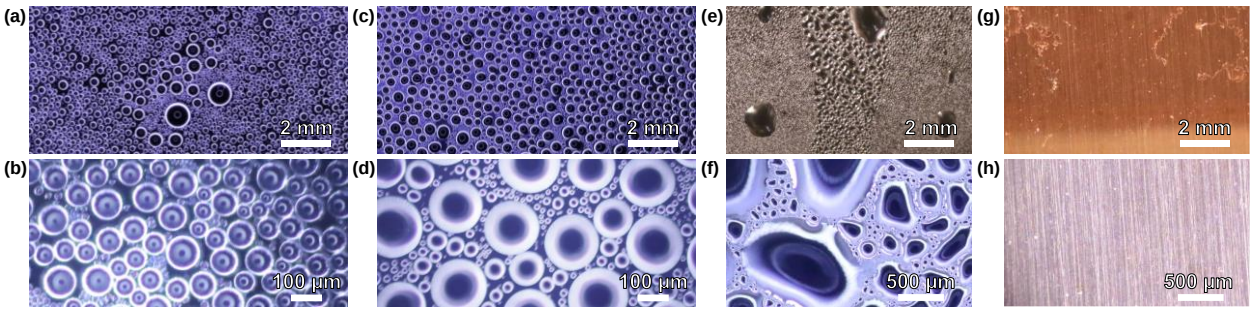

Figure 4. Dropwise condensation on hydrophobic and hydrophilic surfaces. Two exemplary transient droplet size distributions during condensation on a hydrophobic substrate (θ_a / θ_r = 110 ± 4°/102 ± 5°) captured with a DSLR camera coupled to a (a) macro lens and (b) 20X microscope lens. Two exemplary transient droplet size distributions during condensation on our PEGylated hydrophilic substrate (Fig. 3, θ_a/θ_r = 38 ± 1°/35 ± 1°) captured with a DSLR camera coupled to a (c) macro lens and (d) 20X microscope lens. The droplet distributions are self-similar in nature. Two transient droplet size distributions showing quasi-filmwise condensation on a polished silicon substrate (θ_a/θ_r = 46 ± 1°/23 ± 1°) captured with a DLSR camera coupled to a (e) macro lens and (f) 5x microscope lens. Two examples of filmwise condensation on a polished copper substrate (θ_a/θ_r = 97 ± 2°/27 ± 1°) captured with a DLSR camera coupled to a (g) macro lens and (h) 5x microscope lens. Experiments conducted at a condensation heat transfer rate of 930 ± 100 W/m^2.

In order to verify that contact angle hysteresis governs dropwise condensation, we performed two additional tests on surfaces having elevated advancing contact angles with

varying degrees of contact angle hysteresis. The first surface consisted of a polished silicon wafer having advancing and receding contact angles of θ_a = 46 ± 1° and θ_r = 23 ± 1°, respectively ($\Delta\theta \approx 23°$). The droplet morphology during coalescence-mediated droplet growth showed the presence of irregular contact lines, as well as an overall quasi-dropwise condensation process (Fig. 4e, f). Interestingly, a polished copper substrate having a higher advancing contact angle with similar receding angle of θ_a = 97 ± 2° and θ_r = 27 ± 1°, respectively ($\Delta\theta \approx 70°$) showed uniform filmwise condensation (Fig. 4g, h), confirming the minimal role of advancing contact angle on dropwise condensation, and elucidating the importance of contact angle hysteresis.

To quantify the dropwise condensation distribution and to better understand the difference between the self-similar results, we measured the average, i.e. steady state, distribution of droplet sizes on both hydrophobic (Fig. 4, a, b) and hydrophilic (Fig. 4c, d) samples. Figure 5 shows the experimentally measured droplet number density $N(r)$ as a function of droplet radius on our hydrophilic PEGylated surface (blue circles) along with the Rose model with $\hat{r}$ = 0.36 mm [26] (dotted line), valid for dropwise condensation on hydrophobic surfaces having spherical cap shaped droplets. Our experimental data points agree well with the Rose model for multiple decades of droplet size, irrespective of the surface wettability. Figure 5 also shows the experimental maximum droplet radius at the onset of sliding. While theoretical estimation of the maximum departure radius yields $r_{max,th} \approx 1.1$ mm, we did not observe droplet sliding before droplets reached $r_{max,exp}$ = 1.32 mm. The slight discrepancy between model and experiment arises from simplifications made in the model related to contact line shape.

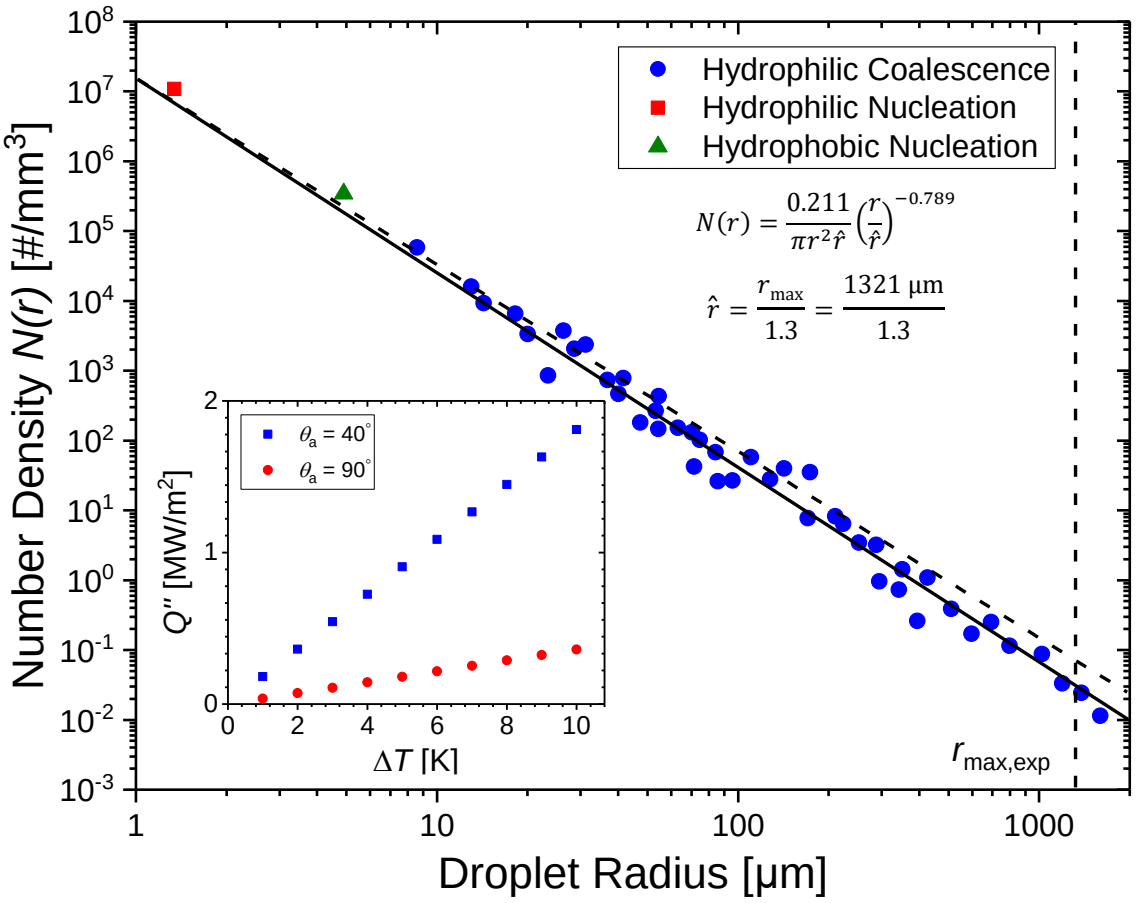

Figure 5. Steady-state droplet size distribution on our hydrophilic PEGylated surface. Dotted line shows the Rose distribution for hydrophobic surfaces with $\hat{r}$ = 0.36 mm, and the solid line shows the fit from the inset equation. The vertical dotted line shows the experimental maximum droplet radius (r_{max} = 1.32 mm). Red symbols indicate the droplet number density at the onset of nucleation for our PEGylated (red square symbol) and hydrophobic (green triangle symbol) surfaces. We estimate the error associated with the automated droplet detection to be less than 10%. Experiments conducted for a condensation heat transfer rate of 930 ± 100 W/m^2. Inset: Model results showing overall surface condensation heat flux (Q'') as a function of vapor-to-surface temperature difference (ΔT) during dropwise condensation of steam on the hydrophobic (red circles) and PEGylated hydrophilic (blue squares) surfaces.

HEAT TRANSFER MODELING

To study the impact of our findings and to quantify the effect of surface hydrophilicity on dropwise condensation heat transfer, we derived a droplet growth model appropriate for hydrophilic dropwise condensation (θ_a < 90°) and combined it with droplet distribution theory using the experimental distribution results for both our PEGylated and hydrophobic surfaces characterized here. As suggested in Figure 1(b), the utilization of a hydrophilic droplet morphology during dropwise condensation shows a 500% heat transfer enhancement when compared to a surface having identical droplet distribution, but with a hydrophobic droplet morphology. Flatter spherical cap shaped droplets enable the minimization of conduction heat transfer resistance through the droplet, which becomes a fundamental bottleneck in dropwise condensation once droplets grow to radii above $R \approx 10$ μm. Indeed, study of the cumulative heat transfer shows that over 90% of the heat removed from a surface occurs by droplets having radii R < 100 μm, putting high importance on minimizing advancing contact angle [27], while maintaining dropwise condensation.

The condensation heterogeneous nucleation rate (J) is:

$$J = N_s C e^{-\frac{\Delta G}{k_B T}}, \tag{1}$$

where N_s the density of nucleation sites on the surface, C is is a constant related to the atomic attachment rate and the Zeldovich factor, and ΔG is the energy barrier for nucleation [28]. For a given surface, N_s is characterized by the surface roughness, with smoother surfaces having lower N. The energy barrier for nucleation (ΔG) is dependent on the condensate-vapor (γ_{lv}), condensate-substrate (γ), and substrate-vapor (γ_{sv}) surface energies:

$$\Delta G = \frac{1}{3}(2 - 3n + n^3)(\pi \gamma_{\mathrm{lv}} {R_{\mathrm{c}}}^2) \tag{2}$$

$$n = (\gamma_{\mathrm{sv}} - \gamma)/\gamma_{\mathrm{lv}} \tag{3}$$

The lower γ, the higher the energy barrier for nucleation (Fig 1a, inset). Hence, two potential mitigation schemes for decreasing scale formation are to: 1) coat the surface with a suitably designed low-surface energy coating (hydrophobic) to increase the energy barrier for nucleation [29-32], and 2) create an atomically smooth interface with minimal roughness to decrease N [33-36].

The heat transfer through an individual hydrophilic droplet (θ_{a} < 90°) was calculated from the analytical solution given by Sadhal and Martin [37]. For hydrophobic droplets (θ_{a} > 90°), to calculate the heat transfer through individual droplets, the numerical solution given by Chavan et. al was used [38]. The individual droplet heat transfer, characterized by the droplet Nusselt number (Nu), is a function of the Biot number (Bi) and apparent advancing contact angle (θ_{a}), *i.e.* $\mathrm{Nu} = f(\mathrm{Bi}, \theta_{\mathrm{a}})$. Here, the Nusselt and Biot numbers are defined in terms of the droplet base radius (R_{b}) as [37]:

$$\mathrm{Bi} = \frac{h_{\mathrm{i}} R_{\mathrm{b}}}{k_{\mathrm{w}}}, \tag{4}$$

$$\mathrm{Nu} = \frac{Q}{k_{\mathrm{w}} R_{\mathrm{b}} (T_{\mathrm{sat}} - T_{\mathrm{s}})}, \tag{5}$$

where Q is the total heat transfer through the droplet and k_{w} is the droplet thermal conductivity. Once Nu is obtained, Q can be calculated from equation (5). The liquid-vapor interface heat transfer coefficient is given by the interfacial condensation heat transfer coefficient, h_{i} [39,40]:

$$h_{\mathrm{i}} = \frac{8\sigma}{2 - 0.798\sigma} \frac{\gamma - 1}{\gamma + 1} \frac{1}{\sqrt{2\pi R_{\mathrm{g}} T_{\mathrm{sat}}}} \frac{h_{\mathrm{fg}}^2}{\nu_{\mathrm{g}} T_{\mathrm{sat}}}, \tag{6}$$

where R_g is the specific gas constant and ν_g is the water vapor specific volume, T_{sat} is the water vapor saturation temperature, h_{fg} is the latent heat of condensation phase change, γ is the Poisson constant, and σ is the condensation coefficient which is taken as, $\sigma = 1$.

To study the overall steady-state condensation heat flux, we combined the individual droplet heat transfer, Q with droplet distribution theory to account for the fraction of droplets on the surface of a given radius R for the surfaces undergoing gravitation shedding and jumping. For small hydrophobic droplets ($R \leq R_e$), the size distribution $n(R)$ is determined by [41]:

$$n(R) = \frac{1}{3\pi R_e^3 \hat{R}} \left(\frac{R_e}{\hat{R}}\right)^{-\frac{2}{3}} \frac{R(R_e - R_{min})}{R - R_{min}} \frac{A_2 R + A_3}{A_2 R_e + A_3} \exp(B_1 + B_2), \tag{7}$$

where $\hat{R}$ is the average maximum droplet radius (departure radius), R_e is the radius when droplets begin to merge and grow by droplet coalescence, R_{min} is the critical nucleation radius for condensing droplets (≈10 nm for water). For large hydrophobic droplets growing due to coalescence ($R \geq R_e$), the droplet distribution $N(R)$ is determined from [42]:

$$N(R) = \frac{1}{3\pi R_e^2 \hat{R}} \left(\frac{R_e}{\hat{R}}\right)^{-\frac{2}{3}}, \tag{8}$$

The variables A_1, A_2, A_3, B_1, B_2 are constants associated with droplet sweeping, defined as [43]:

$$A_1 = \frac{\Delta T}{h_{fg} \rho_w (1 - \cos\theta)^2 (2 + \cos\theta)}, \tag{9}$$

$$A_2 = \frac{\theta}{4 k_w \sin\theta}, \tag{10}$$

$$A_3 = \frac{1}{2h_i(1 - \cos\theta)} + \frac{1}{k_{HC} \sin^2\theta} \left[\frac{k_p \phi}{\delta_{HC} k_p + h k_{HC}} + \frac{k_p (1 - \phi)}{\delta_{HC} k_w + h k_{HC}}\right]^{-1}, \tag{11}$$

$$B_1 = \frac{A_2}{\tau A_1} \left[\frac{R_e^2 - R^2}{2} + R_{min}(R_e - R) - R_{min}^2 \ln\left(\frac{R - R_{min}}{R_e - R_{min}}\right)\right], \tag{12}$$

$$B_2 = \frac{A_3}{\tau A_1}\left[R_{\mathrm{e}} - R - R_{\min}\ln\left(\frac{R - R_{\min}}{R_e - R_{\min}}\right)\right], \tag{13}$$

$$\tau = \frac{3R_e^2(A_2R_{\mathrm{e}} + A_3)^2}{A_1(11A_2R_{\mathrm{e}}^2 - 14R_eR_{\min} + 8A_3R_{\mathrm{e}} - 11A_3R_{\min})}. \tag{14}$$

In our case, the analysis is valid for smooth surfaces (ϕ = 1, h = 0, $\delta_{\mathrm{HC}} \approx 0$) or nanostructured superhydrophobic surfaces ($h \approx 0$, $\delta_{\mathrm{HC}} \approx 0$), A_3 is defined as:

$$A_3 = \frac{1}{2h_{\mathrm{i}}(1 - \cos\theta)}. \tag{15}$$

For hydrophilic droplets, the definition of R_e changes because of the geometry of the hydrophilic droplet and the fact that the droplet base radius, R_b will be related to the nucleation density and not the droplet radius, R:

$$R_{\mathrm{e}} = \frac{1}{4\sin\theta\sqrt{N_{\mathrm{s}}}}. \tag{16}$$

We have an additional $\sin\theta$ term in the denominator. Thus, for hydrophilic droplets (θ_{a} < 90°), Eq. (7) and (8) are modified as:

$$n(R) = \frac{1}{3\pi R_{\mathrm{e}}^3\hat{R}(\sin\theta)^3}\left(\frac{R_{\mathrm{e}}}{\hat{R}}\right)^{-\frac{2}{3}}\frac{R(R_{\mathrm{e}} - R_{\min})}{R - R_{\min}}\frac{A_2R + A_3}{A_2R_{\mathrm{e}} + A_3}\exp(B_1 + B_2), \tag{17}$$

$$N(R) = \frac{1}{3\pi R_{\mathrm{e}}^2\hat{R}(\sin\theta)^3}\left(\frac{R_{\mathrm{e}}}{\hat{R}}\right)^{-\frac{2}{3}}. \tag{18}$$

The total surface steady state condensation heat flux (q") is obtained by incorporating the individual droplet heat transfer rate obtained from literature [37,38], with the droplet size distributions (Eq. 7, 8 for θ_{a} > 90° and Eq. 17 and 18 for θ_{a} < 90°):

$$q" = \int_{R_{\min}}^{R_{\mathrm{e}}} Q(R)n(R)dR + \int_{R_{\mathrm{e}}}^{\hat{R}} Q(R)N(R)dR. \tag{19}$$

To calculate the condensation heat transfer coefficient, h, the heat flux, $q"$ is divided by the temperature difference, ΔT:

$$h = \frac{q"}{\Delta T}. \tag{20}$$

CONCLUSIONS

In summary, we demonstrated the first-ever stable dropwise condensation of steam on hydrophilic surfaces. The experimental data reveals no statistical difference between droplet size distribution for hydrophobic and hydrophilic substrates having low contact angle hysteresis. The discrete droplet formation we observe reinforces a picture where dropwise condensation is governed by contact angle hysteresis and is fundamentally not limited by hydrophobicity or advancing contact angle. The implications of our finding have significant potential. Recent focus by researchers to create droplet-jumping surfaces to remove condensate at micrometer length scales has been fraught with barriers due to progressive surface flooding and high conduction thermal resistance of droplets residing in the spherical superhydrophobic state (Fig. 1a) [44,45]. Our work points to a new direction where tailoring of the contact angle hysteresis, coupled with elevated nucleation density caused by high intrinsic wettability, can potentially enhance condensation heat transfer by 500%. Furthermore, our results prove the ability for an intrinsically wetting solid surface to have high droplet mobility, shedding a light on a new direction for future design of low adhesion coatings and surface processing for a plethora of applications where classically perfluorinated and alkyl based coatings, which are prone to degrade, have been used.

REFERENCES

[0] This thesis is compiled from a previous work by the author: A. Wu, H. Vahabi, H. Cha, S. Chavan, M.-K. Kim, W. Wang, A.K. Kota, N. Miljkovic, Phys Rev Lett, *in review* (2018). © 2018 American Physical Society.

[1] E. Schmidt, W. Schurig, and W. Sellschopp, Z Ver Dtsch Ing **74**, 544 (1930).

[2] J. W. Rose, P I Mech Eng a-J Pow **216**, 115 (2002).

[3] H. Y. Kim, H. J. Lee, and B. H. Kang, J. Colloid Interface Sci. **247**, 372 (2002).

[4] P.-G. d. Gennes, F. Brochard-Wyart, and D. Quéré, *Capillarity and wetting phenomena : drops, bubbles, pearls, waves* (Springer, New York, 2004).

[5] C. Furmidge, Journal of colloid science **17**, 309 (1962).

[6] R. H. Dettre and R. E. Johnson Jr, J Phys Chem **69**, 1507 (1965).

[7] R. E. Johnson Jr and R. H. Dettre, J Phys Chem **68**, 1744 (1964).

[8] R. Dettre, Advances in Chemistry Series **43**, 136 (1964).

[9] D. Kaschiev, *Nucleation: Basic Theory With Applications* (Butterworth Heinemann, Oxford, 2000).

[10] R. Xiao, N. Miljkovic, R. Enright, and E. N. Wang, Sci Rep-Uk **3** (2013).

[11] D. J. Preston, N. Miljkovic, J. Sack, R. Enright, J. Queeney, and E. N. Wang, Appl Phys Lett **105** (2014).

[12] R. Lundy, C. Byrne, J. Bogan, K. Nolan, M. N. Collins, E. Dalton, and R. Enright, ACS Applied Materials & Interfaces **9**, 13751 (2017).

[13] J. W. Rose, Chem Eng Res Des **76**, 143 (1998).

[14] D. J. Preston, N. Miljkovic, J. Sack, R. Enright, J. Queeney, and E. N. Wang, Appl Phys Lett **105** (2014).

[15] R. Lundy, C. Byrne, J. Bogan, K. Nolan, M. N. Collins, E. Dalton, and R. Enright, ACS Applied Materials & Interfaces **9**, 13751 (2017).

[16] H. Y. Cha, A. Wu, M. K. Kim, K. Saigusa, A. H. Liu, and N. Miljkovic, Nano Letters **17**, 7544 (2017).

[17] S. Takeda, M. Fukawa, Y. Hayashi, and K. Matsumoto, Thin Solid Films **339**, 220 (1999).

[18] P. B. Weisensee, Y. B. Wang, H. L. Qian, D. Schultz, W. P. King, and N. Miljkovic, Int J Heat Mass Tran **109**, 187 (2017).

[19] S. Sharma, R. W. Johnson, and T. A. Desai, Biosensors and Bioelectronics **20**, 227 (2004).

[20] T. S. Wong, S. H. Kang, S. K. Y. Tang, E. J. Smythe, B. D. Hatton, A. Grinthal, and J. Aizenberg, Nature **477**, 443 (2011).

[21] T. L. Barr and S. Seal, Journal of Vacuum Science & Technology A: Vacuum, Surfaces, and Films **13**, 1239 (1995).

[22] P. Swift, Surface and Interface Analysis **4**, 47 (1982).

[23] M. K. Kim, H. Cha, P. Birbarah, S. Chavan, C. Zhong, Y. H. Xu, and N. Miljkovic, Langmuir **31**, 13452 (2015).

[24] S. Chavan *et al.*, Langmuir **32**, 7774 (2016).

[25] H. Y. Cha, A. Wu, M. K. Kim, K. Saigusa, A. H. Liu, and N. Miljkovic, Nano Letters **17**, 7544 (2017).

[26] J. W. Rose and L. R. Glicksman, Int J Heat Mass Tran **16**, 411 (1973).
[27] A. Umur and P. Griffith, Journal of Heat Transfer **87**, 275 (1965).
[28] D. Kaschiev, *Nucleation: Basic Theory With Applications* (Butterworth Heinemann, Oxford, 2000).
[29] H. U. Zettler, M. Weiss, Q. Zhao, and H. Muller-Steinhagen, Heat Transfer Eng **26**, 3 (2005).
[30] Q. F. Yang, J. Ding, and Z. Q. Shen, Chem Eng Sci **55**, 797 (2000).
[31] Q. Zhao, Y. Liu, C. Wang, S. Wang, and H. Muller-Steinhagen, Chem Eng Sci **60**, 4858 (2005).
[32] M. Bohnet, Chem-Ing-Tech **57**, 24 (1985).
[33] S. B. Subramanyam, G. Azimi, and K. K. Varanasi, Adv Mater Interfaces **1** (2014).
[34] S. B. Subramanyam, K. Rykaczewski, and K. K. Varanasi, Langmuir **29**, 13414 (2013).
[35] J. D. Smith, R. Dhiman, S. Anand, E. Reza-Garduno, R. E. Cohen, G. H. McKinley, and K. K. Varanasi, Soft Matter **9**, 1772 (2013).
[36] S. Anand, A. T. Paxson, R. Dhiman, J. D. Smith, and K. K. Varanasi, ACS Nano **6**, 10122 (2012).
[37] S. S. Sadhal and W. W. Martin, International Journal of Heat and Mass Transfer **20**, 1401 (1977).
[38] S. Chavan *et al.*, Langmuir **32**, 7774 (2016).
[39] R. W. Schrage, Thesis, Columbia University., 1953.
[40] J. W. Rose, in *Proc. R. Soc. Lond. A* (The Royal Society, 1987), pp. 305.
[41] S. Kim and K. J. Kim, Journal of Heat Transfer **133**, 081502 (2011).
[42] E. J. Le Fevre and J. W. Rose, in *Proceedings of the Third International Heat Transfer Conference* (ASME, Chicago, IL, 1966), pp. 362.
[43] N. Miljkovic, R. Enright, and E. N. Wang, Journal of Heat Transfer **135** (2013).
[44] N. Miljkovic and E. N. Wang, Mrs Bull **38**, 397 (2013).
[45] R. Enright, N. Miljkovic, J. L. Alvarado, K. J. Kim, and J. W. Rose, Nanoscale and Microscale Thermophysical Engineering **8**, 223 (2014).